A theoretical model of cytokinesis implicates feedback between membrane curvature and cytoskeletal organization in asymmetric cytokinetic furrowing

Jonas F. Dorn[a,†], Li Zhang[a], Tan-Trao Phi[a], Benjamin Lacroix[b], Paul S. Maddox[c], Jian Liu[d,*], and Amy Shaub Maddox[c,*]

[a]Institute for Research in Immunology and Cancer, Université de Montréal, Montréal, QC H3T 1J4, Canada; [b]Institut Jacques Monod, 75205 Paris cedex 13, France; [c]Department of Biology, University of North Carolina at Chapel Hill, Chapel Hill, NC 27599; [d]Biochemistry and Biophysics Center, National Heart, Lung, and Blood Institute, National Institutes of Health, Bethesda, MD 20814

ABSTRACT **During cytokinesis, the cell undergoes a dramatic shape change as it divides into two daughter cells. Cell shape changes in cytokinesis are driven by a cortical ring rich in actin filaments and nonmuscle myosin II. The ring closes via actomyosin contraction coupled with actin depolymerization. Of interest, ring closure and hence the furrow ingression are nonconcentric (asymmetric) within the division plane across Metazoa. This nonconcentricity can occur and persist even without preexisting asymmetric cues, such as spindle placement or cellular adhesions. Cell-autonomous asymmetry is not explained by current models. We combined quantitative high-resolution live-cell microscopy with theoretical modeling to explore the mechanistic basis for asymmetric cytokinesis in the *Caenorhabditis elegans* zygote, with the goal of uncovering basic principles of ring closure. Our theoretical model suggests that feedback among membrane curvature, cytoskeletal alignment, and contractility is responsible for asymmetric cytokinetic furrowing. It also accurately predicts experimental perturbations of conserved ring proteins. The model further suggests that curvature-mediated filament alignment speeds up furrow closure while promoting energy efficiency. Collectively our work underscores the importance of membrane–cytoskeletal anchoring and suggests conserved molecular mechanisms for this activity.**

Monitoring Editor
William Bement
University of Wisconsin

Received: Jun 15, 2015
Revised: Feb 11, 2016
Accepted: Feb 16, 2016

INTRODUCTION

Cytokinesis is the physical division of one cell into two. Cell shape changes during this process are accomplished by a temporary cytoskeletal structure known as the contractile ring, which assembles at the cell equator in anaphase (Schroeder, 1972, 1973; Mabuchi and Okuno, 1977; Rappaport, 1996; reviewed by Green *et al.*, 2012). The contractile ring is a specialization of the cortical actomyosin cytoskeleton, which occupies a thin volume beneath the plasma membrane (Schroeder, 1972; Clark *et al.*, 2013). Key components of this ring include the multidomain scaffold protein anillin, the filament-forming septins, minifilaments of nonmuscle myosin II, and formin-dependent, long, unbranched actin filaments (F-actin). Actin filaments are randomly oriented at the equator at the onset of cytokinesis but become circumferentially aligned (Fishkind and Wang, 1993; Noguchi and Mabuchi, 2001; Vavylonis *et al.*, 2008). Actomyosin contraction coupled to actin depolymerization in the plane of the membrane produces contractile force tangential to the membrane, comprising small radial forces that deform the cell cortex into a furrow that ingresses to divide the cell (Schroeder, 1972).

This article was published online ahead of print in MBoC in Press (http://www.molbiolcell.org/cgi/doi/10.1091/mbc.E15-06-0374) on February 24, 2016.

†Present address: Novartis Pharma AG, 4056 Basel, Switzerland.

The authors claim no conflicts of interest.

*Address correspondence to: Jian Liu (jian.liu@nih.gov), Amy Shaub Maddox (asm@unc.edu).

Abbreviations used: F-actin, filamentous actin; myosin II, nonmuscle myosin II.

Furrowing is nonconcentric (asymmetric) in cells throughout Metazoa (Reinsch and Karsenti, 1994; Rappaport, 1996; Das *et al.*, 2003; Alsop and Zhang, 2004; Fleming *et al.*, 2007; Maddox *et al.*, 2007; Kosodo *et al.*, 2008; Carvalho *et al.*, 2009; Bourdages *et al.*, 2014). In most cases, there exists a mechanical asymmetry within the division plane, including intercellular junctions and substrate adhesions, which precedes anaphase. Such features resist furrowing forces and are thus sufficient for asymmetric furrowing (Founounou *et al.*, 2013; Guillot and Lecuit, 2013; Herszterg *et al.*, 2013; Morais-de-Sa and Sunkel, 2013). However, the asymmetry of ring closure can be cell autonomous, as in the *Caenorhabditis elegans* zygote (Audhya *et al.*, 2005; Maddox *et al.*, 2007). How does this asymmetry arise? Initially, a shallow furrow appears relatively synchronously around the division plane (Maddox *et al.*, 2007). As cytokinesis proceeds, the furrow adopts a sharp leading edge at a singular site (Maddox *et al.*, 2007). This feature is perpetuated such that furrowing occurs unilaterally for some time, and the center of the contractile ring is increasingly offset from the center of the division plane (Maddox *et al.*, 2007). The cortex on the opposite side of the division plane (180° from the initial doubled-membrane feature) adopts this sharp curvature only later.

What is the physical mechanism that leads to asymmetric furrowing? Several theoretical models have been used to study the mechanics of cytokinetic ring contraction (Biron *et al.*, 2005; Wang, 2005; Zumdieck *et al.*, 2007; Koyama *et al.*, 2012; Mendes Pinto *et al.*, 2012; Stachowiak *et al.*, 2014; Turlier *et al.*, 2014), and one describes the mechanical differences around the division plane circumference when asymmetry is imposed (Sain *et al.*, 2015). Still, none explains how cell-autonomous asymmetric closure, such as that in the *C. elegans* zygote, arises and persists. The prominent accumulation of ring components on the faster-ingressing side of the furrow was suggested to contribute to asymmetry (Maddox *et al.*, 2007). However, diffusion is predicted to smooth out spatial gradients of protein distribution over the several-minute time course of furrow ingression, and thus this factor is likely insufficient to perpetuate asymmetric furrowing. It therefore remains an open question whether asymmetric furrowing causes or results from localized protein accumulation. Another potential player is the anaphase spindle midzone, which comprises bundled antiparallel microtubules between the segregated chromosomes, contributes to division plane specification, and concentrates many positive regulators of cytokinesis (Douglas and Mishima, 2010). Asymmetric placement of the midzone within the division plane could lead to asymmetric contact with the contractile ring and thus stabilize or amplify asymmetry. However, instead of promoting asymmetry, the midzone was implicated in attenuating asymmetry, since asymmetry decreases when the furrow contacts it (Audhya *et al.*, 2005).

We hypothesize that furrowing is nonconcentric via the action of a cortex-intrinsic positive feedback mechanism that perpetuates an initial, stochastic asymmetry. We consider the unique doubled-membrane furrow leading edge as a candidate for the initial asymmetry. By light microscopy, this feature is diffraction limited (Maddox *et al.*, 2005); the radius of membrane curvature is likely <150 nm. Here we propose that high membrane curvature influences the alignment of associated cytoskeletal filaments. That is, for filaments to maximize their association with the membrane and bind without buckling, it is energetically favorable for filaments to align circumferentially along the furrow instead of orthogonally to it. Filament alignment in turn facilitates actomyosin contractility, which further drives furrowing. This concept of membrane curvature–mediated cytoskeletal organization forms the key element in a positive feedback loop among filament alignment, contractility, and membrane curvature.

Here we combine theoretical modeling and experiments to test this idea. Our model predicts that curvature-mediated cytoskeletal organization is essential to recapitulate the observed asymmetric furrow ingression; this prediction is corroborated by experimental perturbations of conserved contractile ring components. The model further suggests functional roles of these proteins and indicates that the asymmetry of furrowing trades off with speed to achieve a maximum energy efficiency of cytokinesis in different cell types. Thus our model encompasses a concept that can explain asymmetric furrowing, describes the mechanics of the contractile ring, and begins to assign molecular identity to these activities. Of importance, we propose a novel contributor to contractile ring mechanics: the influence of local membrane curvature on cytoskeletal organization via filament–membrane attachment.

RESULTS

Model development

Here we present a theoretical model that aims to explain the sustained asymmetry of contractile ring closure in the *C. elegans* zygote. The model describes the mechanical contraction of the contractile ring and its coupling with the furrowing plasma membrane. The central notion of the model is that membrane curvature in the furrow affects the alignment of the cytoskeletal filaments in the contractile ring, which in turn governs the contractility that further drives furrowing (Figure 1A). We propose that this curvature-mediated feedback loop perpetuates the symmetry breaking arising from random fluctuations and underlies asymmetric furrow ingression (Figure 1B).

The model describes the cytokinetic furrow ingression without explicit representation of individual molecules. To discern the mechanism underlying asymmetric furrowing, the model comprehensively integrates key components, including the cortical cytoskeleton, the membrane, and the spindle midzone. It builds upon the energy arising from interactions among these key players. We first depict the model qualitatively and then formulate the quantitative model.

Although strict sarcomeric organization has not been observed in cytokinetic contractile rings, several lines of evidence support the idea that the contractile ring comprises a collection of "contractile units" (Bement and Capco, 1991; Carvalho *et al.*, 2009; Pollard, 2010). Motivated by this evidence, we modeled the contractile ring as a circle of connected contractile segments bound to the interior of a membrane tubule, which is 50 µm long with a diameter of 30 µm (Figure 1C), similar to the dimensions of the *C. elegans* zygote. Within each segment, an ensemble of myosin II bipolar minifilaments spans two groups of actin filaments (Burns *et al.*, 1995a,b; Yumura *et al.*, 2008; Zhou and Wang, 2008; Vale *et al.*, 2009), which occupy the two circumferential ends of each segment (adjacent to adjoining segments). The external, barbed ends of the actin filaments can be thought of as connected to the neighboring segment by actin cross-linkers, which are represented by the spring-like connections between the segments. Thus the ring segments resemble the sarcomeres of muscle or stress fibers. However, unlike in sarcomeres, the actin filaments within each ring segment begin with random orientation (not aligned) and align progressively with time and as the cytokinetic furrow ingresses (Figure 1C).

The model posits that actin filament alignment within each ring segment arises from two sources. First, we propose that the local membrane curvature favors the circumferential orientation of actin filaments (Figure 1A). This is because when the membrane is flat, filaments can fully attach to the membrane in any orientation (Mukhina *et al.*, 2007; Reichl *et al.*, 2008; Skau *et al.*, 2011), whereas the maximization of filament-membrane binding favors circumferential filament alignment with the furrow when the cortex is curved. We termed this phenomenon curvature-dependent

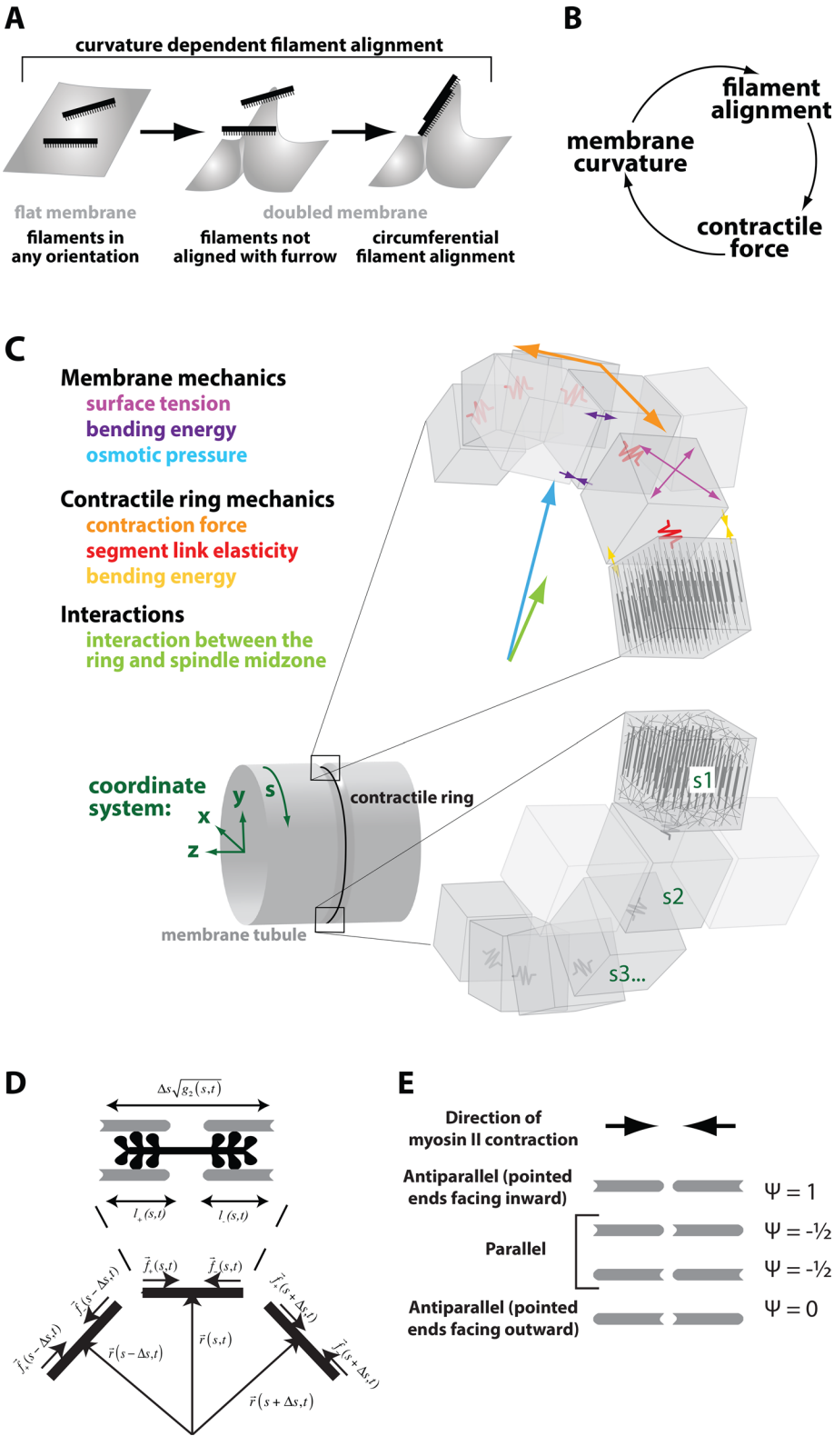

FIGURE 1: Schematics of a theoretical model featuring membrane curvature–mediated feedback between filament alignment and contraction in asymmetric furrowing. (A) A key model concept is curvature-dependent filament alignment. Membrane curvature favors filament alignment along the furrow. (B) Positive feedback loop among local filament alignment, contractile force, and membrane curvature. (C) Model layout and coordinate system. (D) Magnified view of sarcomere-like ring segment described in the model and considerations of force generation within segments and contraction effects on neighboring segments. (E) Schematics of order parameter for filament alignment.

filament alignment. In addition, F-actin cross-linkers bundle filaments and promote their alignment regardless of the local membrane shape (Mukhina *et al.*, 2007; Reichl *et al.*, 2008; Skau *et al.*, 2011). We further assume that filament alignment facilitates filament sliding and, hence, the contractility of each ring segment. This hypothesis is in part supported by the observation that antiparallel filament orientation potentiates contraction (Reymann *et al.*, 2010). Consequently, contractility coupled with actin depolymerization drives segment shortening and ring closure (Schroeder, 1972; Medeiros *et al.*, 2006; Haviv *et al.*, 2008; Carvalho *et al.*, 2009; Wilson *et al.*, 2010; Mendes Pinto *et al.*, 2012). This shortening and the associated inward movement of ring segments further drive the local membrane shape change, thus closing the curvature-mediated positive feedback loop (Figure 1B). On the other hand, aligned, cross-linked F-actin (i.e., an F-actin bundle) is much stiffer than an isotropic meshwork (Gardel *et al.*, 2004; Shin *et al.*, 2004; Claessens *et al.*, 2006). The progressive filament alignment thus also increases the bending resistance of the contractile ring segment, thus opposing the local contractility. Although contractile ring ingression is also opposed by membrane resistance and a resistive force representing the spindle midzone, both of these factors are of relatively low magnitude compared with that of ring rigidity (see model parameter consideration in the Supplemental Material). Thus furrow ingression consists of five tightly coupled subprocesses: filament alignment, sliding, and depolymerization, the displacement of the spindle midzone upon contact with the ring, and membrane shape changes.

Formulation of the quantitative model

We first construct the total energy function of the contractile apparatus F, which sums the mechanical energy of the system and free energy changes arising from the ordering of the F-actin within each ring segment:

$$F = \underbrace{F_{\text{Membrane mechanics}} + F_{\text{Ring mechanics}}}_{\text{Mechanical energy}} + \underbrace{F_{\text{Phase ordering}}}_{\text{Free energy from filament alignment}} \quad (1)$$

The mechanical energy includes membrane mechanics, the mechanics of the contractile ring, and the interaction between the contractile ring and the midzone spindle. We consider that filament alignment within the contractile ring is a phase transition process. The associated free energy change is

modeled as a continuous phase transition and described by the "ϕ–4 theory," which is used to characterize phase transitions in soft condensed matter such as liquid crystals (Landau and Lifshitz, 1980). We construct our model in a discrete form in order to faithfully represent actomyosin contractility (see Section I in the Supplemental Material for detailed reasons and Table 1 for term definitions). Later we will elaborate on each energy contribution.

$$F_{\text{Membrane mechanics}} = \sum_{z=-\frac{Nz}{2}}^{\frac{Nz}{2}} \sum_{s=1}^{Ns} \sqrt{g_3(s,z,t)} \left\{ \underbrace{\kappa_1 C_M^2}_{\text{Bending energy from mean curvature}} + \underbrace{\sigma}_{\text{Surface tension}} + \underbrace{\frac{1}{2}(x_s y - x y_s) P_0}_{\text{Osmotic pressure}} \right\} \tag{2}$$

Equation 2 describes the membrane mechanical energy, which is Helfrich-like membrane energy in its continuum limit, and includes contributions of bending energy, surface tension, and osmotic pressure. Throughout the model, a cylindrical coordinate system is used. The membrane tubule is divided into $N_z + 1$ parts along the z-axis (the pole-to-pole axis) and N_s segments in the radial direction, where s stands for the sth membrane patch in the radial direction (Figure 1C). Under this coordinate system, the position of the membrane patch $\vec{r}(s,z,t) = \big(x(s,z,t), y(s,z,t)\big)$ is represented as a function of s, z, and time t. From the differential geometry, the mean curvature of the local membrane is $C_M = \frac{1}{2g_3^{1.5}}\big[(x_{ss}y_s - x_s y_{ss})\big(1 + x_z^2 + y_z^2\big) + \big(x_s^2 + y_s^2\big)(x_{zz}y_s - x_s y_{zz}) - 2(x_s x_z + y_s y_z)(x_{sz}y_s - x_s y_{sz})\big]$

Here $g_3(s,z,t) = x_s^2 + y_s^2 + (x_s y_z - x_z y_s)^2$. Finally, all of the expressions of derivatives are in discrete form; for example, the partial derivative of x with regard to s is $x_s = \frac{1}{2}\big(x(s+1) - x(s-1)\big)$. We have

sth ring segment (Figure 1D). In addition, because actin cross-linkers connect the ring segments, force balance dictates that this mismatch within the ring segment could stretch or compress these cross-linkers between the neighboring ring segments (see Sections II and III in the Supplemental Material for detailed parameter derivation together with references). A mismatch between the myosin II minifilament length $\sqrt{g_2(s,t)}$ and actin filament length $l(s,t)$ (Figure 1D) could thus incur an energy penalty, approximated by $\frac{1}{2}K_1\Big(\sqrt{g_2(s,t)} - l(s,t)\Big)^2$ in the model. The local curvature of the ring is $C_R = (x_{ss}y_s - x_s y_{ss}) / g_2^{1.5}$, and the position of the spindle midzone is denoted as $\vec{r}_m$.

$$F_{\text{Free energy from filament alignment}} = \sum_{s=1}^{Ns} \big\{ D\psi_s^2(s,t) + (a_0 + AC_G)\psi^2(s,t) + B\psi^4(s,t) \big\} \tag{4}$$

Equation 4 represents the free energy change from filament ordering. The order parameter ψ(s) is a normalized value that describes the level of F-actin alignment ordering within each ring segvment. We provide a detailed physical derivation of ψ(s) in Section I in the Supplemental Material. Briefly, $\psi > 0$ when filaments are antiparallel with pointed ends facing toward each other, $\psi < 0$ for those in parallel, and $\psi = 0$ when filaments are in total disorder (Figure 1E). Of importance, two terms in Eq. 4 drive the filament

$$F_{\text{Ring mechanics}} = \sum_{s=1}^{Ns} \left[\underbrace{\left\{ \frac{1}{2}\Big(\vec{f}_+(s,t) l_+(s,t) \cdot \big(\vec{r}(s+1,t) - \vec{r}(s-1,t)\big) - \vec{r}(s,t) \cdot \big(\vec{f}_+(s+1,t) l_+(s+1,t) + \vec{f}_-(s-1,t) l_-(s-1,t) \big) \Big) \right\}}_{\text{Contraction}} \right] + \sum_{s=1}^{Ns} \underbrace{\frac{1}{2} K_1 \Big(\sqrt{g_2(s,t)} - l(s,t) \Big)^2}_{\text{Ring segment connectivity}} + \underbrace{\frac{1}{2}\kappa_3 \sqrt{g_2(s,t)} C_R^2}_{\text{Ring bending energy}} + \underbrace{\frac{1}{2} K_2 \big| \vec{r}(s,t) - \vec{r}_m(t) \big|^2}_{\text{Interaction between ring and midzone spindle}} \tag{3}$$

Equation 3 characterizes the contractile ring mechanics, including the contraction, connectivity, bending, and ring–midzone spindle interaction. Here $\vec{f}_+(s,t)l_+(s,t)$ and $\vec{f}_-(s,t)l_-(s,t)$ are the internal contractile forces on the left and right ends for the sth segment, respectively (Figure 1D). In addition, $\vec{f}_+(s,t) + \vec{f}_-(s,t) = 0$ and $\big|\vec{f}_+(s)\big| = \big|\vec{f}_-(s)\big| = f(s)$, where $f(s)$ has the unit of force per length and $l_+(s,t) = l_-(s,t) = \frac{1}{2}l(s,t)$, where $l(s,t)$ is the length of the actin filaments overlapping with the myosin II heads within the ring segment. Because the ring is constitutively attached to the membrane at the equator ($z = 0$), the model dictates that the position of the sth ring segment is the same as that of the corresponding membrane patch. The position of the ring segment is similarly represented as

$$\vec{r}(s,z,t) = \big(x(s,z,=0,t), y(s,z=0,t)\big)$$

which is reduced to $\vec{r}(s,t) = \big(x(s,t), y(s,t)\big)$ for simplicity. Here $g_2(s,z=0,t) = x_s^2 + y_s^2$, and $\sqrt{g_2(s,t)}$ is the end-to-end length of the

alignment order parameter ψ. First, the term a_0 represents the energetically favorable filament bundling driven by F-actin cross-linkers; a_0 is a negative constant, driving filament alignment regardless of local membrane shape. Second, the term AC_G specifically drives filament alignment via local Gaussian curvature C_G (Figure 1A), where

$$C_G = g_3^{-2}\Big[(x_{ss}y_s - x_s y_{ss})(x_{zz}y_s - x_s y_{zz}) - (x_{sz}y_s - x_s y_{sz})^2 \Big]$$

A represents the effective filament–membrane binding energy, which is positive (see Sections I and III in the Supplemental Material for detailed derivation). At the local furrow (negative local Gaussian curvature), the term AC_G turns negative, and thus curvature-dependent filament alignment is favorable (Figure 1A). In addition, the term D in the phase ordering free energy represents the energy penalty for spatial variation in ψ, thus promoting the uniform ordering in filament alignment along the ring perimeter. The fourth-order term is positive and an entropy term that favors disorder in filament alignment.

Term	Definition
A	Coefficient of curvature-dependent free energy change for filament alignment
a_0	Curvature-independent free energy change for filament alignment
α	Inhibitory effect on contractility by the spindle midzone
B	Coefficient of the fourth-order term in the filament alignment free energy change associated with entropy
C_G	Gaussian curvature of the local membrane
C_M	Mean curvature of the local membrane
C_R	Local curvature of the contractile ring
D	Energy penalty for spatial variation in the order parameter ψ
$E_{\text{attachment}}$	Attachment energy (free energy) when a filament is fully attached to the membrane
F	Total energy of the furrowing system
$F_{\text{Membrane mechanics}}$	Energy contribution of membrane mechanics
$F_{\text{Phase ordering}}$	Free energy change from filament alignment
$F_{\text{Ring mechanics}}$	Energy contribution of ring mechanics
$f(s)$	Internal contractile forces for the sth ring segment (sum of forces on both sides of the segment, f_+ and f_-)
f_0	Maximal contractile force per unit length
$g_2(s)$	End-to-end length of the sth ring segment
$g_3(s, z)$	Surface area of the local membrane patch at (s, z)
K_1	Spring constant of the linkage between adjacent ring segments
K_2	Spring constant of midzone-ring repulsion potential
κ_1	Membrane bending modulus
κ_3	Bending modulus of contractile ring
$l(s)$	Length of actin filaments overlapping with myosin II heads in the sth ring segment (sum of overlap on both sides of the segment, l_+ and l_-)
λ_1	Viscous drag coefficient for ring contraction
λ_2	Viscous drag coefficient for filament shrinkage
λ_3	Viscous drag coefficient for filament alignment
λ_4	Viscous drag coefficient for spindle midzone displacement
N_S	Number of segments in the radial direction
N_Z	Number of membrane tubule sections along the z-axis
P_0	Osmotic pressure
$\psi(s)$	Order parameter for filament alignment within the sth ring segment
$\vec{r}(s)$	Position of the midzone spindle in (x, y, z) coordinates
$\vec{r}_m$	Position of the sth ring segment in (x, y, z) coordinates
s	Spatial coordinate along the radial direction of the ring or the membrane tubule
σ	Membrane surface tension
x	Cartesian coordinate along x-axis
y	Cartesian coordinate along y-axis
z	Cartesian coordinate along z-axis
ξ	White Gaussian noise in filament alignment level

TABLE 1: Definitions for all terms appearing in main text equations.

Critically, the local filament ordering affects the contractility $f(s)$ and the stiffness of the ring segment κ_3. Specifically,

$$f(s) = f_0 \cdot \left(\psi(s) + |\psi(s)|\right) \cdot \left(1 - \frac{\alpha}{R_0}\left|\vec{r}(s,t) - \vec{r}_m\right|\right)$$

and $\kappa_3 = \kappa_3^{(0)}|\psi|$. Here $f(s)$ is assumed to be proportional to (ψ + $|\psi|$): only the organization in which filaments are antiparallel with pointed ends facing toward each other ($\psi > 0$) can confer productive myosin II contraction; f_0 is the maximum contractile force per unit length; and R_0 is the original radius of the ring. The α term

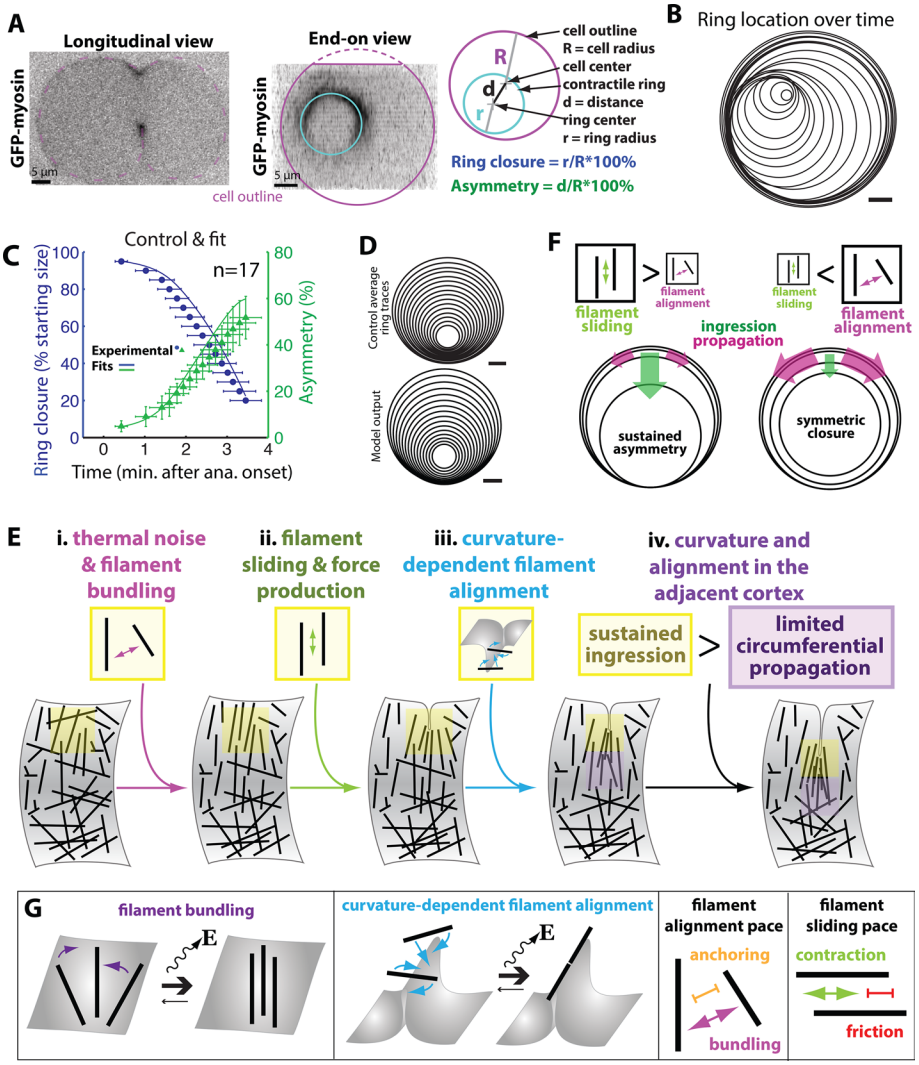

FIGURE 2: Quantitative analysis of contractile ring kinetics and geometry is recapitulated by the theoretical model. (A) The *xy* and *xz* views of a control *C. elegans* zygote expressing green fluorescent protein (GFP)–tagged myosin II and schematics and equations summarizing measurements of ring closure kinetics. (B) Example location of cytokinetic ring over time in a control cell. Scale bars, 5 μm. (C) Experimental (points; bars = SD) and model output (lines) plots of ring closure and concentricity with respect to time. The model parameter values that recapitulate the dynamics of furrow ingression in control cells are listed in the Model Parameter Table in the Supplemental Model Description. These model parameters remain fixed throughout model calculations, unless otherwise noted. (D) Averaged, aligned ring position at 5% closure intervals for control *C. elegans* embryos and model output of ring size and position over 5% closure intervals. (E) Schematics of asymmetric furrowing, initiated by thermal noise and stochastic local filament bundling and amplified by the positive feedback loop introduced in Figure 1B. Bottom, schematics depicting a patch of equatorial cortex and actomyosin cytoskeletal filaments (black lines). Right-pointing arrows reflect time. (F) The balance between the relative rates of filament sliding and alignment dictates the symmetry of furrow ingression. When filament sliding is faster than filament alignment, the resulting ingression outcompetes the circumferential propagation of filament alignment, leading to asymmetric furrow ingression. Conversely, symmetric furrow ingression ensues when filament sliding is slower than filament alignment. (G) Key model parameters: filament bundling, curvature-dependent filament alignment, filament alignment rate, and filament sliding rate.

represents the chemical inhibitory effect on contraction from the spindle midzone (Miller and Bement, 2009).

The dynamics of the system is governed by the functional derivative of the total energy by variations of the position ($\vec{r}$) and the filament ordering (ψ) of the ring segment/corresponding membrane patch, and the position of the spindle midzone ($\vec{r}_m$; see Eqs. 5–8). Because the shrinkage of actin filament length $l(s)$ is an active process, it is assumed to be directly driven by the local contraction (see Section I in the Supplemental Material for detailed theoretical considerations). The λ_i ($i = 1$–4) in the following equations are the effective viscous drag coefficients for ring contraction and membrane shape change (λ_1), filament shrinkage (λ_2), filament alignment (λ_3), and midzone spindle displacement (λ_4), respectively:

$$\lambda_1 \frac{\partial \vec{r}(s,z,t)}{\partial t} = -\frac{\delta F}{\delta \vec{r}(s,z,t)} \tag{5}$$

$$\lambda_2 \frac{\partial l(s,t)}{\partial t} = -f\left(\psi(s,t)\right)\sqrt{g_2(s,t)} \tag{6}$$

$$\lambda_3 \frac{\partial \psi(s,t)}{\partial t} = -\frac{\delta F}{\delta \psi(s,t)} + \zeta(s,t) \tag{7}$$

$$\lambda_4 \frac{\partial \vec{r}_m(s,z,t)}{\partial t} = -\frac{\delta F}{\delta \vec{r}_m(s,z,t)} \tag{8}$$

To calculate furrowing dynamics, we numerically integrate Eqs. 5–8 over time from the initial state in which filament orientation is random and contraction force is zero, the midzone is centered on the origin, and the membrane tubule is at mechanical equilibrium. We consolidated all of the randomness of the system into the phase ordering process in Eq. 7 by a white Gaussian noise $\left(\langle\zeta(s,t)\rangle = 0 \text{ and } \langle\zeta(s_1,t_1)\zeta(s_2,t_2)\rangle = |\zeta_0|^2\,\delta(s_1-s_2)\delta(t_1-t_2)\right)$. At each time step, the model reports the state of the system by the position of each membrane patch and midzone spindle and the position, the length, and the filament ordering level of each ring segment.

The key model result of asymmetric furrowing is robust against variations of the model parameters (Supplemental Figure S1). It emerges as a natural consequence of the curvature-dependent filament alignment, largely independent of specific model parameter values.

The theoretical model recapitulates asymmetric furrowing of the *C. elegans* zygote when contraction is faster than filament alignment

We first tested whether our model based on a simple mechanical feedback loop can recapitulate experimentally observed kinetics and geometry of cytokinesis. We performed high-resolution three-dimensional time-lapse imaging of *C. elegans* zygotes and measured contractile ring size and position over time (Figure 2, A–C, and Supplemental Movie S1; Dorn *et al.*, 2010; Bourdages *et al.*, 2014). Our model was able to recapitulate three aspects of the kinetics of cytokinesis in vivo (Figure 2, C and D): initiation timing, closure

duration, and nonconcentricity. According to our model, actin filaments are initially randomly oriented ($\psi = 0$ everywhere). The model assumes that a small and constant driving force ($a_0 < 0$ in Eq. 4) promotes circumferential filament alignment. Thermal fluctuations, however, seed the initial heterogeneity in ψ along the perimeter (Figure 2Ei). As more filaments become locally aligned, actomyosin contraction becomes more efficient (Figure 2Eii). The resulting stronger contraction drives a deeper furrow ingression, the larger Gaussian curvature of which locally promotes a greater filament alignment that in turn facilitates even more local contractions (Figure 2Eiii). Thus the local curvature mediates positive feedback between the cytoskeletal organization that facilitates force generation and the resulting furrow ingression, amplifying asymmetry.

For the initial asymmetric furrow to be perpetuated, our model predicts that the pace of filament sliding (and thus ring contraction) is faster than the filament alignment pace. This is because when the furrow starts to ingress locally, the membrane curvature of the adjacent region will gradually increase, in turn locally promoting filament alignment. Thus filament alignment, contraction, and furrowing will spread circumferentially from the initial furrowing site to the entire ring (Figure 2Eiv). Only when the rate of filament alignment is much slower than that of ring contraction can the initial asymmetry be amplified and sustained far into furrow ingression (Figure 2F). We thus found that four of the model parameters were critically important in dictating the dynamics of ring contraction: the free energy gains from filament bundling and for curvature-dependent filament alignment and the rates of filament alignment and sliding (Figure 2G). More specifically, whereas the free energy gains for filament bundling and curvature-dependent filament alignment (a_0 and A in Eq. 4) promote ring closure, closure dynamics is slowed by the associated viscous drag coefficients of the dynamic processes (λ_1 in Eq. 5 and λ_3 in Eq. 7).

The nature of contractile ring actin influences furrow asymmetry

The model predicts that when contraction is slow relative to filament alignment, the initial ingression propagates more quickly around the cell circumference and eliminates the initial asymmetry (Figure 2F). To test this model prediction in vivo, we depleted the protein ARX-2, a member of the well-characterized, conserved Arp2/3 complex, which regulates the actin cytoskeleton in many contexts (Firat-Karalar and Welch, 2011) and was implicated in negative regulation of contractility during cytokinesis (Moulding *et al.*, 2007; Canman *et al.*, 2008) but whose depletion or mutation does not grossly alter contractile events in the zygote (Severson *et al.*, 2002). We reasoned that perturbing this complex would alter the equilibrium between dendritic and unbranched F-actin; the latter is more amenable to bundling and sliding (Yang *et al.*, 2012). In the model, this perturbation corresponds to a comparatively faster rate of filament alignment (a smaller viscous drag coefficient λ_3 in Eq. 7), which results in faster circumferential propagation of the initial ingression and more-symmetric furrowing (Figure 3A). Indeed, ring closure is more symmetric in cells depleted of Arp2/3 (Figure 3A). These results are consistent with our model prediction that the balance between the paces of filament alignment and contraction dictates asymmetry in vivo. Fitting the model to the Arp2/3 depletion also required higher energy gains from filament bundling, in agreement with the abundance of long filaments with extensive alignment (Figure 3D). Fitting also required reduced energy gains from curvature-dependent filament alignment, which may reflect an increased cross-linking activity that outcompetes and hence decreases F-actin binding to the membrane. This effect is also consistent with the decrease in the rate of filament sliding, which could relate to the assumption that when longer filaments are aligned, they share more bundling cross-links, which inhibit sliding.

This agreement between theory and experiments suggests that sustained asymmetry requires furrow ingression (which is mediated by contraction) to be dominant over circumferential furrow propagation (driven by filament alignment).

Conserved contractile ring proteins govern the kinetics and asymmetry of furrow ingression

The conserved structural contractile ring components myosin II, anillin, and the septins are proposed to contribute to contraction, cytoskeletal cross-linking, and anchoring of the cytoskeleton to the membrane. These activities could influence both the energy and the dynamics of the contractile apparatus (Figure 3A) and hence the feedback among filament alignment, contractile force, and membrane curvature. To further test our model predictions and functionally annotate contractile ring proteins, we next analyzed the changes in the four critical parameters required to fit the phenotypes resulting from the depletion of these conserved proteins. The four critical parameters are 1) the free energy gain from curvature-independent filament alignment, a_0 in Eq. 1; 2) the free energy gain from curvature-dependent filament alignment, A in Eq. 1; 3) the viscous drag coefficient for ring contraction, λ_1 in Eq. 2; and 4) the viscous drag coefficient for filament alignment, λ_3 in Eq. 4 (Figure 2G).

Anillin is a multidomain protein implicated in coupling the actomyosin cytoskeleton to the plasma membrane directly (Liu *et al.*, 2012) or via the septins (Piekny and Maddox, 2010). The septins form hetero-oligomeric complexes, filaments, and sheets in association with the plasma membrane (Kinoshita *et al.*, 2002; Mostowy and Cossart, 2012). Septins directly bind anillin and myosin II and create curved F-actin bundles (Kinoshita *et al.*, 2002; Joo *et al.*, 2007; Mavrakis *et al.*, 2014). Our model predicts that reducing membrane–cytoskeleton attachment decreases the free energy gain from curvature-dependent filament alignment (a smaller A in Eq. 1), increases the rate of filament alignment due to reduced membrane friction (a smaller λ_3), and decreases contraction pace (a smaller λ_1), since anchoring is needed to translate contractility into furrow ingression (Figure 3, B and D). By decreasing the energy incentive for curvature-mediated filament alignment, the reduction in membrane–cytoskeleton attachment compromises curvature-mediated positive feedback. Consequently the membrane curvature resulting from furrowing does not influence filament alignment locally. As a result, curvature-independent filament alignment dominates, circumferential filament alignment is more uniform, and furrowing is more symmetric (Figure 3, B and C, solid lines).

Indeed, depletion of anillin or the septins results in concentric ring closure (Figure 3, B and C; Maddox *et al.*, 2007). We fitted the model to three aspects of experimental ring closure dynamics and geometry: initiation timing, duration of closure, and asymmetry. Fitting the model to measurements from cells depleted of anillin or of the septins required varying the four critical model parameters (Figure 3D; see later discussion). As predicted for decreased cytoskeleton–membrane coupling, curvature-dependent filament alignment was made less energetically favorable (smaller A) and the filament alignment pace was increased (smaller λ_3). The necessary decrease in the filament sliding rate (larger λ_1) could be conferred by a reduction in cytoskeleton–membrane attachment. This model result demonstrates the necessity of curvature-mediated positive feedback for asymmetric furrow ingression. In addition, these results support the idea that anillin and the septins contribute to cytokinesis by coupling actomyosin to the membrane (Piekny and Maddox, 2010; Saarikangas and Barral, 2011; Liu *et al.*, 2012).

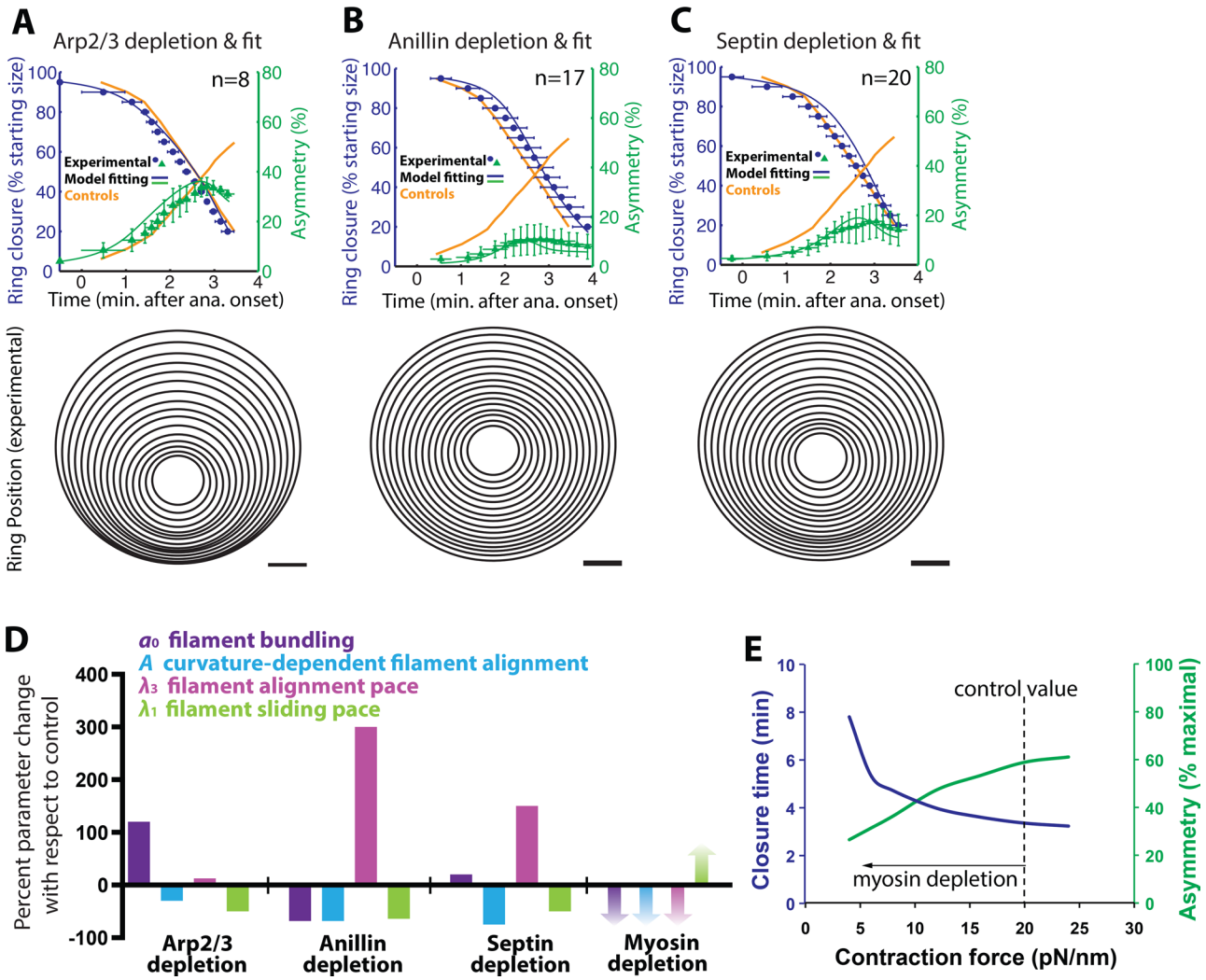

FIGURE 3: Conserved cytoskeletal components are required for asymmetric furrowing. (A–C) Top, contractile ring closure kinetics and geometry were measured (points + SD) for *C. elegans* zygotes depleted of ARX-2 (A; Arp2; Arp2/3 complex), ANI-1 (B; anillin), or UNC-59 and UNC-61 (C; septins). Bottom, averaged, aligned ring position at 5% closure intervals. (D) Graphical representation of variations applied to the four tunable parameters that were performed for model fittings. For myosin II, shaded arrows represent conceptual differences from controls. (E) To address the contributions of myosin II to ring closure, asymmetry and closure time were calculated for the operation of the theoretical model of the ring for a range of contraction force. Varying force only is predicted to decrease asymmetry while increasing closure time.

Of interest, anillin and septin depletions have opposite effects on furrow initiation timing: septin depletion allows earlier initiation, whereas anillin depletion causes a delay (Maddox *et al.*, 2007; Figure 3, B and C). To recapitulate the kinetics as well as the asymmetry results of the two perturbations, we made opposite alterations of one model parameter. To fit anillin depletion ring closure kinetics, we made filament bundling less energetically favorable (a_0 in Eq. 4 is less negative; Figure 3D), indicating that anillin's F-actin–bundling activity (Field and Alberts, 1995; Maddox *et al.*, 2005; Dorn *et al.*, 2010) is important for its contributions to ring closure dynamics. Indeed, anillins bundle F-actin in vitro (Supplemental Figure S2A; Field and Alberts, 1995; Kinoshita *et al.*, 2002). In contrast, an increase in free energy gain from filament bundling (a_0 in Eq. 4 is more negative) is necessary to recapitulate the earlier initiation resulting from septin depletion (Figure 3D). The reduction of membrane binding–based friction, overabundance of myosin II (Supplemental Figure S2B; Maddox *et al.*, 2007), and lack of effect on anillin recruitment (Supplemental Figure S2C) likely facilitate bundling when septins are depleted.

Myosin II is believed to drive contractile ring closure by actomyosin filament sliding or processively cross-linking depolymerizing actin filaments (Green *et al.*, 2012; Ma *et al.*, 2012; Mendes Pinto *et al.*, 2012). Consequently myosin II inhibition could be expected to reduce the rate of contraction (i.e., larger viscous drag coefficient λ_1 or, equivalently, smaller contraction force f_0) and thus cause slower, more-symmetric furrowing (Figure 3E). Instead, although partial myosin II inhibition by depletion of the myosin light chain activator Rho kinase predictably delays furrow initiation and slows ingression, it in fact increases furrow asymmetry (Piekny and Mains, 2002; Maddox *et al.*, 2007). In addition, depletion of NOP-1, a condition also believed to decrease activity of Rho effectors, results in markedly asymmetric furrowing (Tse *et al.*, 2012). Our model suggests that increased asymmetry can result from an exaggerated increase in the rate of contraction relative to that of filament alignment (smaller

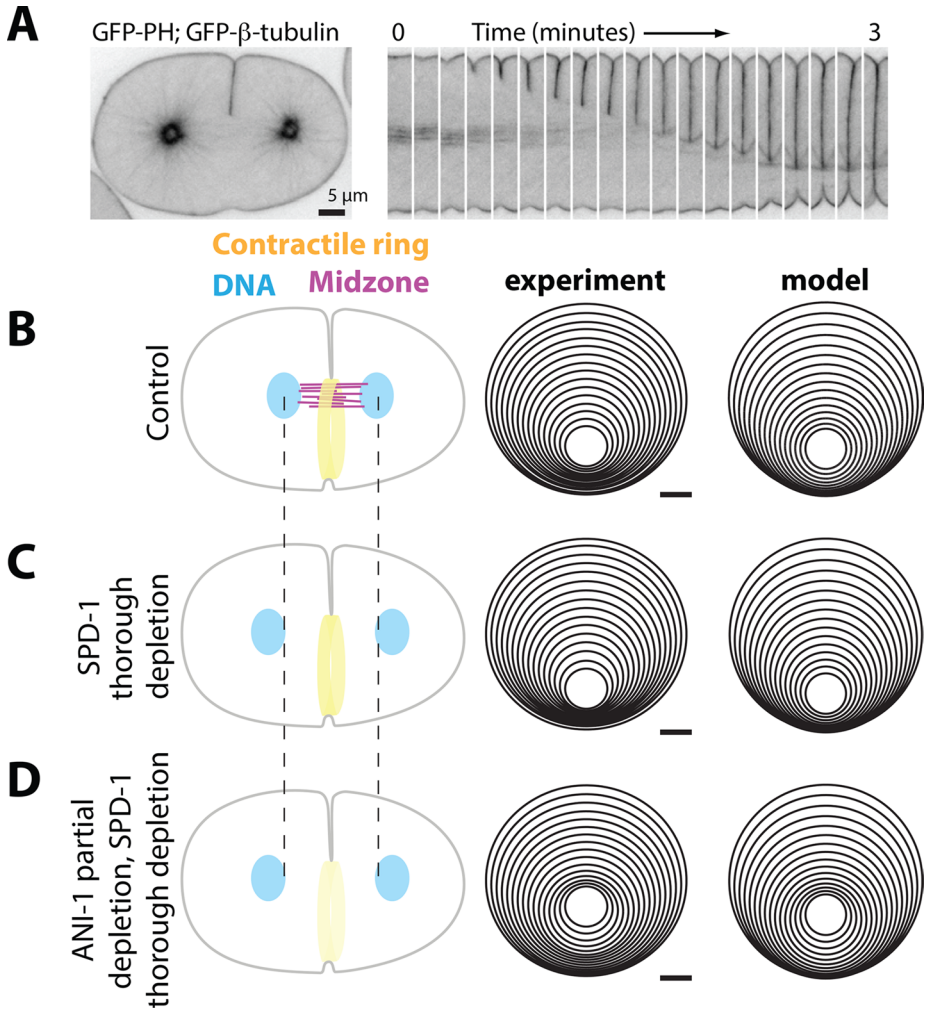

FIGURE 4: The spindle midzone is a weak barrier to contractile ring ingression. (A) The ingressing furrow and spindle midzone are visible in a *C. elegans* embryo expressing a GFP-tagged plasma membrane probe (Audhya *et al.*, 2005) and GFP-tagged tubulin. The furrow displaces the midzone microtubules from the center of the division plane. (B–D) Left, schematics illustrating perturbations of the midzone (pink), contractile ring (yellow), and chromosome (blue) segregation. Vertical dashed lines denote normal centroids of control daughter nuclei. Center, averaged, aligned positions of the contractile ring at 5% closure intervals for control *C. elegans* zygotes (B; repeated from Figure 2D for ease of comparison) and those thoroughly depleted of SPD-1 (C) or simultaneously thoroughly depleted of SPD-1 and partially depleted of ANI-1 (D). Right, model output of ring closure kinetics and geometry for control cells (B), those lacking internal resistance representing the midzone (C), or those lacking the midzone and decreased membrane–cytoskeleton attachment (D). For model result in C, the mechanical interaction with and the chemical inhibition effect on the contractile ring, that is, K_2 in Eq. 3 and the α term in the contractile force, are set to zero. For model result in D, in addition to the model parameter changes in C, other parameter alterations are similar to that in Figure 3, B and D, to mimic the effect of anillin depletion.

λ_1/λ_3; Figure 3, D and E). One way in which myosin II inhibition could cause this imbalance is if myosin II contributes not only to contraction, but also to filament alignment. In support of this idea, myosin II exists in the contractile ring as bipolar filaments (Yumura *et al.*, 2008; Zhou and Wang, 2008; Vale *et al.*, 2009; Beach *et al.*, 2014) that robustly bundle actin in vitro (Reymann *et al.*, 2010; Thoresen *et al.*, 2011). In addition, myosin II, like other actin bundlers, could slow filament sliding and hence contraction by generating friction (Janson *et al.*, 1992; Mukhina *et al.*, 2007). Partial inhibition of myosin II would thus be predicted to reduce friction and impede filament alignment and therefore increase the contraction speed relative to that of filament alignment. In sum, due to the increased asymmetry seen after myosin II inhibition, our model suggests dual roles for myosin II in cytokinesis: driving contractility and bundling actin.

The geometry of furrowing is largely intrinsic to the cortex

The spindle midzone comprises antiparallel bundled microtubules and lies in the center of the division plane. A nonconcentric furrow encounters the midzone when it is approximately half closed (Figure 4A). On impact, the midzone may attenuate the asymmetry of the furrow by physically resisting its ingression or it may boost asymmetry because it harbors activators of contractility. Our model predicts that the asymmetry of furrow ingression is largely intrinsic to the cell cortex since the forces exerted by the contractile ring are much larger than those holding the midzone in place (Supplemental Material). In silico, the ring closes asymmetrically even in the absence of resistive forces representing the spindle midzone (Figure 4, B and C). Indeed, the midzone is readily displaced upon impact with the furrow in control cells (Figure 4A). To test whether the midzone attenuates asymmetry, we depleted the microtubule bundler SPD-1, eliminating midzone microtubule bundles but not blocking cytokinesis completion (Verbrugghe and White, 2004; Figure 4B and Supplemental Figure S3, A and B). Furrow asymmetry is slightly higher in SPD-1–depleted cells than in controls (Figure 4, B and C, and Supplemental Figure S3A), suggesting that the midzone is a weak barrier to furrow ingression. Therefore the midzone is not necessary for asymmetry.

The furrow can initiate asymmetrically but terminate close to the center of the division plane (it can recenter) after perturbation of cortical proteins (Figure 3). Although our model suggests that asymmetry is intrinsic to the cortex, recentering could result from the balance of forces between the cortex and midzone. We directly tested whether recentering requires resistance by the midzone or can occur in the absence of midzone bundles. We combined thorough depletion of SPD-1 with a cortical perturbation that elicits recentering (partial depletion of anillin; Supplemental Figure S3, C and D). Alteration of the cortical cytoskeleton was thus sufficient to dictate the geometry of ring closure (recentering), even in the absence of a midzone barrier (Figure 4D and Supplemental Figure S3D). Therefore we conclude that ring geometry is primarily dictated by cortical players.

Asymmetric furrowing increases energy efficiency

We previously showed that reduction of active myosin II causes failure of symmetric cytokinesis, even though asymmetric furrowing can succeed in this condition (Maddox *et al.*, 2007). We thus

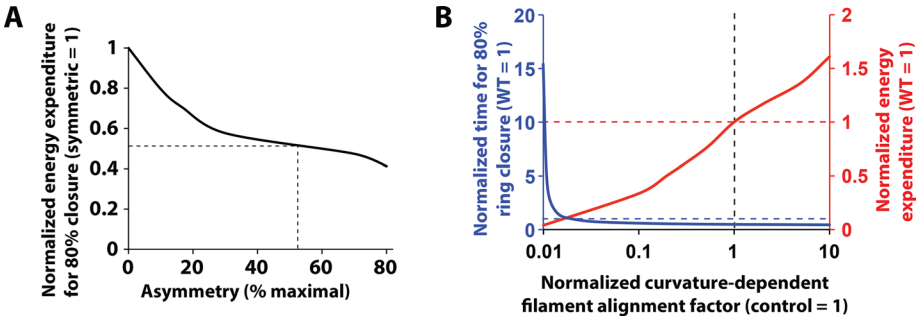

FIGURE 5: Speed trades off with energy efficiency for cytokinetic furrow ingression. (A) Model calculation shows that the energy expenditure decreases with the asymmetric factor of furrow ingression. Here increased asymmetry results from the relative increase of the rate of filament sliding as compared with that of filament alignment. (B) Model calculation shows that the free energy gain for curvature-dependent filament alignment speeds up the furrow ingression but increases the energy expenditure at the same time.

hypothesized that symmetric furrowing requires more energy than asymmetric closure. We tested this hypothesis computationally by integrating the total energy expenditure for contractile ring closure in scenarios of different relative rates of filament sliding and alignment while keeping other model factors unchanged. That is, we numerically calculated the work done during furrowing by integrating the driving force of filament contraction (the right-hand side of Eq. 1) times the displacements of the ring over time. We found that asymmetric furrow closure is ~50% more energy efficient than symmetric furrow closure (Figure 5A). Although filament alignment facilitates contraction, it also increases the rigidity of the cortical cytoskeleton and consequently the bending resistance within the contractile ring. In a symmetric contractile ring, where alignment is uniformly high, ingression thus costs more energy. This suggests that the relationship between the paces of filament alignment and of sliding, which dictates the asymmetry of furrow ingression, determines the energy efficiency of cytokinesis.

Energy efficiency of furrow ingression trades off with speed

Energy efficiency is unlikely to be the only factor that influences cell behavior. In embryos, speed is of the essence, cell cycles are short, and cell division events are fast, as compared with their counterparts in somatic cells. We leveraged our model to test whether removing the constraint of closure speed could reveal a more energy-efficient mode. We reduced curvature-dependent filament alignment (i.e., decreasing the value of A in Eq. 4 while keeping all of the other parameters the same) such that curvature-mediated positive feedback is eliminated (while keeping all other factors unchanged). With decreased A, the energy efficiency of ingression increases (Figure 5B, red trace). Decreasing the curvature-dependent filament alignment factor A by 100 times from that for the control causes ring closure to take more than six times longer than in the *C. elegans* zygote (Figure 5B, blue trace), longer than the entire *C. elegans* embryonic cell cycle (Deppe *et al.*, 1978) but fully compatible with the kinetics of cytokinesis in somatic cells. In this mode, ring closure is relatively symmetric (Figure 5A). In cells, this likely corresponds to a broad contractile apparatus such as that of mammalian and *Drosophila* cultured cells, which yields a very small Gaussian curvature at the furrowing site. The model further reveals that, although the energy gain from curvature-dependent filament alignment greatly increases furrowing speed, it also increases energy cost (Figure 5B, red trace). The model thus suggests that the strength of curvature-dependent filament alignment dictates different modes of cytokinetic furrow ingression in different cell types, where speed trades off with energy efficiency.

DISCUSSION

A novel model for cytokinesis implementing membrane curvature–dependent cytoskeletal organization explains asymmetric furrowing

Here we investigate the physical mechanism of cytokinetic ring closure. Our model based on mechanical feedback among filament alignment, contraction, and membrane curvature recapitulates not only the kinetics of cytokinesis but also its asymmetry, a phenomenon that is ubiquitous but unexplained in its cell-autonomous instances. Central to the feedback is curvature-dependent filament alignment (Figure 1A). Furthermore, protein-based membrane–cytoskeleton linkers (e.g., anillin and the septins) are essential for this feedback, as they govern the relationship between the paces of contraction and filament alignment and consequently the balance between furrow ingression and furrow propagation. This balance, rather than differences in overall mechanism, likely accounts for the observed differences in the geometry of ring closure among cell types.

Of interest, while not consistently observed, a subset of controls contains cells that display spiraling movement of the cytokinetic ring center in addition to asymmetric furrowing (Supplemental Figure S4). To date, our theoretical model has not been able to recapitulate this large-scale spiral movement of the ring center. This is because the model describes membrane as an elastic sheet and imposes that the ring segment and the membrane patch to which it attaches share the same spatial position. The observed spiral movement reflects the ring rotation, which in reality likely entails dissociation between the ring segment and the local membrane and/or rearrangements of the associated membrane patches in the plane of the membrane. The present model cannot describe either of these two events sufficient for ring rotation. In particular, the in-plane rearrangement of membrane patches requires the lateral movement of lipids in the membrane plane. It is hydrodynamic in nature, which cannot be faithfully described by the elastic illustration in the model, which assumes that membrane patches do not rearrange their relative position. This intriguing spiraling phenomenon thus warrants future investigation.

The model allows functional annotation of conserved contractile ring proteins

The simplicity of our model and absence of protein-based agents allow an unbiased investigation of protein function. Because we found that the mechanics of cytokinesis is largely intrinsic to the cortical cytoskeleton, we focused on annotating several conserved ring components—anillin, septins, and myosin II—which have been proposed to have multiple, overlapping functions. Fitting the model to the kinetics of three independent experimental readouts (initiation timing, closure duration, and asymmetry) upon protein perturbations allows us to make specific mechanistic hypotheses about the roles of these ring components in membrane–cytoskeleton coupling, filament bundling, and contractility.

Anillin, a large multidomain protein that binds many cytokinetic ring components, has engendered myriad hypotheses for its mode of action (Piekny and Maddox, 2010). Our model suggests that

anillin contributes to actomyosin filament alignment, likely via its F-actin–bundling domain but also possibly by linking F-actin with active myosin II (Field and Alberts, 1995; Straight *et al.*, 2005). Model fitting also suggests that anillin contributes to cytoskeleton–membrane linkage. Indeed, anillin bears a lipid-binding PH domain (Liu *et al.*, 2012) and can bind the septins (Kinoshita *et al.*, 2002). An important role in cytoskeleton–membrane linkage may explain the division plane instability in anillin-depleted cultured mammalian and *Drosophila* cells (Piekny and Maddox, 2010). Although these roles are not unexpected, our work suggests that this particular behavior is a major factor in how anillin contributes to contractile ring function.

Septins' roles in metazoan cytokinesis are poorly defined and hypothesized based on their in vitro activities and roles elsewhere. As linear and grid-like polymers, they could aid cytoskeleton alignment. As membrane associated proteins, they could link the cytoskeleton to the membrane. In most organisms, many septin proteins and isoforms are expressed and likely form multiple combinatorial complexes (Sellin *et al.*, 2011). In *C. elegans*, a single heterotetrameric species is believed to be formed from the only two septin proteins (John *et al.*, 2007), and septin function can be completely removed with a single molecular perturbation (Nguyen *et al.*, 2000). Our model suggests that septins are important for membrane–cytoskeletal linkage. This proposition is consistent with the role of septins in bleb retraction (Gilden *et al.*, 2012).

Our model suggests that myosin II not only provides contractility, but it also contributes significantly to actin cross-linking and bundling. This result likely relates to the fact that the myosin II in contractile ring is in the form of bipolar minifilaments (Yumura *et al.*, 2008; Beach *et al.*, 2014). Myosin II's cross-linking activity has been implicated in providing the driving force for cytokinetic furrowing (Yumura *et al.*, 2008; Mendes Pinto *et al.*, 2012; Beach *et al.*, 2014). Going forward, it will be important to uncover the relative contributions of myosin II's multiple activities.

Together these results demonstrate the power of our model in annotating the functions of conserved contractile components.

Further considerations of curvature-mediated positive feedback

The key factor of our model is that the curvature of the furrow is both the cause and the result of contractile ring constriction and furrow ingression, that is, curvature-mediated positive feedback. With a minimal model describing the essential elements of the system, we recapitulated furrow asymmetry with a positive feedback loop mediated by curvature-dependent filament alignment. This feedback concept is based on the energy consideration that actin filaments maximize their attachment to the membrane and free energy is reduced when filaments orient circumferentially along the furrow (Figure 1A). The model assumes that the actin filaments are straight throughout their length but could buckle with a 300-nm radius of curvature (Murrell and Gardel, 2012). Consequently they could partially conform to the high curvature at the furrowing site (likely <150-nm radius of curvature) and align transversely across the furrow. Nevertheless, filament buckling is energetically unfavorable. Thus our proposed configuration of straight actin filaments with circumferential alignment has a relatively lower free energy and is more favorable. Future work will be aimed at precisely measuring furrow curvature and its relationship to local cytoskeletal orientation.

Other factors could contribute to the curvature-mediated positive feedback. For instance, curvature-stabilizing proteins may respond to and further stabilize the membrane curvature at the furrowing site. These include proteins containing F-BAR domains (Shlomovitz and Gov, 2008) or amphipathic helices or that form curved polymers, such as septins (Kinoshita *et al.*, 2002; Tanaka-Takiguchi *et al.*, 2009). These factors could thus take part in driving cytokinesis by promoting the positive feedback loop we propose here.

Myosin II has been shown to contract more powerfully in response to mechanical load (Cremo and Geeves, 1998; Veigel *et al.*, 2003; Kovas *et al.*, 2007). Increased filament alignment due to bundling or curvature-dependent filament alignment would allow engagement of more myosin II heads on actin and thus more load. This could in turn lead to more powerful myosin II contraction, potentially myosin II filament growth (Ren *et al.*, 2009), and deeper ingression. Therefore load-sensitive contractility would participate in the same feedback loop we propose.

One model to explain different modes of cytokinesis

Asymmetric furrowing occurs in most, but not all, popular model species. Most prominently, budding and fission yeast exhibit symmetric ring closure (Bi *et al.*, 1998; Wu *et al.*, 2003). This behavior is predicted by our model: within the parameter ranges tested, when the diameter of the cell is <5 μm, circumferential propagation of the initial asymmetric furrow completes so quickly that furrowing becomes symmetric (Supplemental Figure S1C). In addition, circumferential furrow propagation may be favored by cytoskeletal arrangement; in budding and fission yeasts, the septin and actomyosin cytoskeletons, respectively, become circumferentially aligned before the onset of ring closure (Vrabioiu and Mitchison, 2006; Vavylonis *et al.*, 2008). According to our model, this phenomenon corresponds to filament bundling outpacing filament sliding, which results in symmetric furrowing.

Asymmetric furrowing is an energy-efficient way to perform fast cytokinesis, according to our model. Speed is very important in embryonic systems. Indeed, many species' embryos exhibit asymmetric furrowing. Whereas in the *C. elegans* zygote the mechanical feedback loop may be sufficient to initiate asymmetric furrowing, in other systems, such as the ctenophore zygote, supplementary mechanisms including eccentric spindle placement account for asymmetry. For epithelial cells in a monolayer, mechanical resistance by apical junctional complexes biases the effectiveness of equatorial contractility to the basolateral cell surface (reviewed by Bourdages and Maddox, 2013). Similarly, remnant substrate adhesions likely locally attenuate furrowing upward from the coverslip during asymmetric furrowing in cultured human and *Drosophila* cells (Bourdages *et al.*, 2014). In all of these cases, the feedback loop we propose likely contributes to the maintenance of asymmetry. In future work, it will be interesting to examine furrowing kinetics and geometry in somatic cultured cells in mechanical isolation. Given the conservation of the structural proteins implicated in our positive feedback loop, we expect that in such cells, furrowing will be measurably asymmetric even in the absence of extrinsic cues.

MATERIALS AND METHODS

See the Supplemental Experimental Procedures for further considerations of the theoretical model.

C. elegans maintenance and sample preparation

C. elegans were maintained according to standard procedures at 20°C. Strains used were JJ1473 (Munro *et al.*, 2004; Carvalho *et al.*, 2009) and OD122 (Dorn *et al.*, 2010). See Supplemental Table S1 for full genotypes. Embryos were dissected from gravid hermaphrodites and mounted under coverslips on agarose cushions as in Gonczy *et al.* (1999).

Live-cell imaging

A Nikon TE-2000 inverted microscope equipped with a swept field real-time confocal module (Prairie Technologies [Bruker], Middleton, WI) and CoolSNAP HQ2 charge-coupled device camera (Photometrics, Tucson, AZ) was used. The use of the 70-µm slit, a 60× oil-immersion objective (with 2 × 2 binning), and a 200-ms exposure time was kept constant for all embryos of a given strain.

RNA interference

Protein depletion by RNA-mediated interference (RNAi) was performed as done previously (Maddox *et al.*, 2005, for injection; Kamath *et al.*, 2001, for feeding). Bacterial strains for RNAi feeding were obtained from a whole-genome RNAi library (Kamath *et al.*, 2003). See Supplemental Table S2 for primer sequences.

Image and data analysis

Ring geometry was determined using cyanRing (for cytokinesis analysis of the contractile ring; Dorn *et al.*, 2010; Bourdages *et al.*, 2014), a semiautomated software tool written in Matlab (MathWorks, Natick, MA). cyanRing allows rectangular cropping with arbitrary orientation of the equatorial region of the embryo. This region is rotated and maximum projected to produce a view of the contractile ring along the spindle axis in the posterior direction. The user then defines the cell outline, as well as the outline of the contractile ring, by selecting at least three points, through which best-fit circles are drawn. Ring geometry is then calculated as shown in Supplemental Figure 2A.

Not all depletions exhibited 100% penetrance. To characterize the depletion phenotype rather than the degree of penetrance, we did not include data for cells that were indistinguishable from controls. Including these data with those of affected cells would have yielded a population average that does not reflect either the perturbation or the control. In addition, outlier data points were discarded, such as an apparent increase in the size of the contractile ring to more than the cell size, that are nonphysiological and most likely due to human error in annotating images. To avoid stylizing the data, the analysis pipeline does not allow reannotating the images.

To average data, the time of anaphase onset was determined by visual inspection of the data and set to zero. This assignment has an error of up to 10 s (our sampling frequency). Owing to this error, averaging per time point would result in a population average for closure with an artifactually low slope. By contrast, ring size measurements are comparatively more reliable: the maximum speed of ring closure is very similar among cells within a condition. To avoid introducing error by averaging per time point, we instead averaged at specific intervals of relative ring closure. Because ring closure occurs smoothly, we used linear interpolation to find the time at which specific ring closure percentages were reached and calculated average and SD for 5% ring-closure intervals (5, 10,..., 90, 95%) using custom, publically available code (ch.mathworks.com/matlabcentral/fileexchange/27134-plot-average-line). Because the values for ring closure percentage have been imposed, no uncertainties are reported for them. Data for asymmetry and time were averaged across curves, and their experimental variability was calculated as the SD.

The 5% closure intervals of cell-biological and theoretical data averages were plotted as series of circles with the measured or calculated radii, respectively. The displacement between the center of the cell or a cytokinetic ring time point and the previous time point (the nonconcentricity) was given an arbitrary, consistent direction (downward from the center of the cell).

ACKNOWLEDGMENTS

We thank Kerry Bloom, Julie Canman, and Ewa Paluch for critical reading of the manuscript. Carlos Patino Descovich and all members of the Maddox labs provided discussion and support. Jean-Claude Labbé provided feeding RNAs. James Fethiere (Institute for Research in Immunology and Cancer, Montreal, Canada) provided purified protein fragments. We acknowledge the thoughtful and constructive input from the anonymous referees. J.F.D. was supported by a postdoctoral fellowship from the Swiss National Science Foundation. This work was supported by National Institutes of Health Grant GM102390 to A.S.M. J.L. is supported by the intramural research program of the National Heart, Lung, and Blood Institute at the National Institutes of Health.

REFERENCES

Alsop GB, Zhang D (2004). Microtubules continuously dictate distribution of actin filaments and positioning of cell cleavage in grasshopper spermatocytes. J Cell Sci 117, 1591–1602.

Audhya A, Hyndman F, McLeod IX, Maddox AS, Yates JR 3rd, Desai A, Oegema K (2005). A complex containing the Sm protein CAR-1 and the RNA helicase CGH-1 is required for embryonic cytokinesis in Caenorhabditis elegans. J Cell Biol 171, 267–279.

Beach JR, Shao L, Remmert K, Li D, Betzig E, Hammer JA 3rd (2014). Nonmuscle myosin II isoforms coassemble in living cells. Curr Biol 24, 1160–1166.

Bement WM, Capco DG (1991). Analysis of inducible contractile rings suggests a role for protein kinase C in embryonic cytokinesis and wound healing. Cell Motil Cytoskeleton 20, 145–157.

Bi E, Maddox P, Lew DJ, Salmon ED, McMillan JN, Yeh E, Pringle JR (1998). Involvement of an actomyosin contractile ring in Saccharomyces cerevisiae cytokinesis. J Cell Biol 142, 1301–1312.

Biron D, Alvarez-Lacalle E, Tlusty T, Moses E (2005). Molecular model of the contractile ring. Phys Rev Lett 95, 098102–098104.

Bourdages KG, Lacroix B, Dorn JF, Descovich CP, Maddox AS (2014). Quantitative analysis of cytokinesis in situ during C. elegans postembryonic development. PLoS One 9, e110689.

Bourdages KG, Maddox AS (2013). Dividing in epithelia: cells let loose during cytokinesis. Dev Cell 24, 336–338.

Burns CG, Larochelle DA, Erickson H, Reedy M, De Lozanne A (1995a). Single-headed myosin II acts as a dominant negative mutation in Dictyostelium. Proc Natl Acad Sci USA 92, 8244–8248.

Burns CG, Reedy M, Heuser J, De Lozanne A (1995b). Expression of light meromyosin in Dictyostelium blocks normal myosin II function. J Cell Biol 130, 605–612.

Canman JC, Lewellyn L, Laband K, Smerdon SJ, Desai A, Bowerman B, Oegema K (2008). Inhibition of Rac by the GAP activity of centralspindlin is essential for cytokinesis. Science 322, 1543–1546.

Carvalho A, Desai A, Oegema K (2009). Structural memory in the contractile ring makes the duration of cytokinesis independent of cell size. Cell 137, 926–937.

Claessens MMAE, Bathe M, Frey E, Bausch AR (2006). Actin-binding proteins sensitively mediate F-actin bundle stiffness. Nat Mater 5, 748–753.

Clark AG, Dierkes K, Paluch EK (2013). Monitoring actin cortex thickness in live cells. Biophys J 105, 570–580.

Cremo CR, Geeves MA (1998). Interaction of actin and ADP with the head domain of smooth muscle myosin: implications for strain-dependent ADP Release in smooth muscle. Biochemistry 37, 1969–1978.

Das T, Payer B, Cayouette M, Harris WA (2003). In vivo time-lapse imaging of cell divisions during neurogenesis in the developing zebrafish retina. Neuron 37, 597–609.

Deppe U, Schierenberg E, Cole T, Krieg C, Schmitt D, Yoder B, von Ehrenstein G (1978). Cell lineages of the embryo of the nematode Caenorhabditis elegans. Proc Natl Acad Sci USA 75, 376–380.

Dorn JF, Zhang L, Paradis V, Edoh-Bedi D, Jusu S, Maddox PS, Maddox AS (2010). Actomyosin tube formation in polar body cytokinesis requires Anillin in C. elegans. Curr Biol 20, 2046–2051.

Douglas ME, Mishima M (2010). Still entangled: assembly of the central spindle by multiple microtubule modulators. Semin Cell Dev Biol 21, 899–908.

Field CM, Alberts BM (1995). Anillin, a contractile ring protein that cycles from the nucleus to the cell cortex. J Cell Biol 131, 165–178.

Firat-Karalar EN, Welch MD (2011). New mechanisms and functions of actin nucleation. Curr Opin Cell Biol 23, 4–13.

Fishkind DJ, Wang YL (1993). Orientation and three-dimensional organization of actin filaments in dividing cultured cells. J Cell Biol 123, 837–848.
Fleming ES, Zajac M, Moschenross DM, Montrose DC, Rosenberg DW, Cowan AE, Tirnauer JS (2007). Planar spindle orientation and asymmetric cytokinesis in the mouse small intestine. J Histochem Cytochem 55, 1173–1180.
Founounou N, Loyer N, Le Borgne R (2013). Septins regulate the contractility of the actomyosin ring to enable adherens junction remodeling during cytokinesis of epithelial cells. Dev Cell 24, 242–255.
Gardel ML, Shin JH, MacKintosh FC, Mahadevan L, Matsudaira P, Weitz DA (2004). Elastic behavior of cross-linked and bundled actin networks. Science 304, 1301–1305.
Gilden JK, Peck S, Chen YC, Krummel MF (2012). The septin cytoskeleton facilitates membrane retraction during motility and blebbing. J Cell Biol 196, 103–114.
Gonczy P, Schnabel H, Kaletta T, Amores AD, Hyman T, Schnabel R (1999). Dissection of cell division processes in the one cell stage Caenorhabditis elegans embryo by mutational analysis. J Cell Biol 144, 927–946.
Green RA, Paluch E, Oegema K (2012). Cytokinesis in animal cells. Annu Rev Cell Dev Biol 28, 29–58.
Guillot C, Lecuit T (2013). Adhesion disengagement uncouples intrinsic and extrinsic forces to drive cytokinesis in epithelial tissues. Dev Cell 24, 227–241.
Haviv L, Gillo D, Backouche F, Bernheim-Groswasser A (2008). A cytoskeletal demolition worker: myosin II acts as an actin depolymerization agent. J Mol Biol 375, 325–330.
Herszterg S, Leibfried A, Bosveld F, Martin C, Bellaiche Y (2013). Interplay between the dividing cell and its neighbors regulates adherens junction formation during cytokinesis in epithelial tissue. Dev Cell 24, 256–270.
Janson LW, Sellers JR, Taylor DL (1992). Actin-binding proteins regulate the work performed by myosin II motors on single actin filaments. Cell Motil Cytoskeleton 22, 274–280.
John CM, Hite RK, Weirich CS, Fitzgerald DJ, Jawhari H, Faty M, Schlapfer D, Kroschewski R, Winkler FK, Walz T, *et al*. (2007). The Caenorhabditis elegans septin complex is nonpolar. EMBO J 26, 3296–3307.
Joo E, Surka MC, Trimble WS (2007). Mammalian SEPT2 is required for scaffolding nonmuscle myosin II and its kinases. Dev Cell 13, 677–690.
Kamath RS, Fraser AG, Dong Y, Poulin G, Durbin R, Gotta M, Kanapin A, Le Bot N, Moreno S, Sohrmann M, *et al*. (2003). Systematic functional analysis of the Caenorhabditis elegans genome using RNAi. Nature 421, 231–237.
Kamath RS, Martinez-Campos M, Zipperlen P, Fraser AG, Ahringer J (2001). Effectiveness of specific RNA-mediated interference through ingested double-stranded RNA in Caenorhabditis elegans. Genome Biol 2, 1–10.
Kinoshita M, Field CM, Coughlin ML, Straight AF, Mitchison TJ (2002). Self- and actin-templated assembly of mammalian septins. Dev Cell 3, 791–802.
Kosodo Y, Toida K, Dubreuil V, Alexandre P, Schenk J, Kiyokage E, Attardo A, Mora-Bermudez F, Arii T, Clarke JD, *et al*. (2008). Cytokinesis of neuroepithelial cells can divide their basal process before anaphase. EMBO J 27, 3151–3163.
Kovas M, Thirumurugan K, Knight PJ, Sellers JR (2007). Load-dependent mechanism of nonmuscle myosin 2. Proc Natl Acad Sci USA 104, 9994–9999.
Koyama H, Umeda T, Nakamura K, Higuchi T, Kimura A (2012). A high-resolution shape fitting and simulation demonstrated equatorial cell surface softening during cytokinesis and its promotive role in cytokinesis. PLoS One 7, e31607.
Landau LD, Lifshitz EM (1980). Statistical Physics, Oxford, UK: Butterworth Heinemann.
Liu J, Fairn GD, Ceccarelli DF, Sicheri F, Wilde A (2012). Cleavage furrow organization requires PIP(2)-mediated recruitment of anillin. Curr Biol 22, 64–69.
Ma X, Kovacs M, Conti MA, Wang A, Zhang Y, Sellers JR, Adelstein RS (2012). Nonmuscle myosin II exerts tension but does not translocate actin in vertebrate cytokinesis. Proc Natl Acad Sci USA 109, 4509–4514.
Mabuchi I, Okuno M (1977). The effect of myosin antibody on the division of starfish blastomeres. J Cell Biol 74, 251–263.
Maddox AS, Habermann B, Desai A, Oegema K (2005). Distinct roles for two C. elegans anillins in the gonad and early embryo. Development 132, 2837–2848.
Maddox AS, Lewellyn L, Desai A, Oegema K (2007). Anillin and the septins promote asymmetric ingression of the cytokinetic furrow. Dev Cell 12, 827–835.
Mavrakis M, Azou-Gros Y, Tsai FC, Alvarado J, Bertin A, Iv F, Kress A, Brasselet S, Koenderink GH, Lecuit T (2014). Septins promote F-actin ring formation by crosslinking actin filaments into curved bundles. Nat Cell Biol 16, 322–334.
Medeiros NA, Burnette DT, Forscher P (2006). Myosin II functions in actin-bundle turnover in neuronal growth cones. Nat Cell Biol 8, 216–226.
Mendes Pinto I, Rubinstein B, Kucharavy A, Unruh JR, Li R (2012). Actin depolymerization drives actomyosin ring contraction during budding yeast cytokinesis. Dev Cell 22, 1247–1260.
Miller AL, Bement WM (2009). Regulation of cytokinesis by Rho GTPase flux. Nat Cell Biol 11, 71–77.
Morais-de-Sa E, Sunkel C (2013). Adherens junctions determine the apical position of the midbody during follicular epithelial cell division. EMBO Rep 14, 696–703.
Mostowy S, Cossart P (2012). Septins: the fourth component of the cytoskeleton. Nat Rev Mol Cell Biol 13, 183–194.
Moulding DA, Blundell MP, Spiller DG, White MR, Cory GO, Calle Y, Kempski H, Sinclair J, Ancliff PJ, Kinnon C, *et al*. (2007). Unregulated actin polymerization by WASp causes defects of mitosis and cytokinesis in X-linked neutropenia. J Exp Med 204, 2213–2224.
Mukhina S, Wang YL, Murata-Hori M (2007). Alpha-actinin is required for tightly regulated remodeling of the actin cortical network during cytokinesis. Dev Cell 13, 554–565.
Munro E, Nance J, Priess JR (2004). Cortical flows powered by asymmetrical contraction transport PAR proteins to establish and maintain anterior-posterior polarity in the early C. elegans embryo. Dev Cell 7, 413–424.
Murrell MP, Gardel ML (2012). F-actin buckling coordinates contractility and severing in a biomimetic actomyosin cortex. Proc Natl Acad Sci USA 109, 20820–20825.
Nguyen TQ, Sawa H, Okano H, White JG (2000). The C. elegans septin genes, unc-59 and unc-61, are required for normal postembryonic cytokineses and morphogenesis but have no essential function in embryogenesis. J Cell Sci 113, 3825–3837.
Noguchi T, Mabuchi I (2001). Reorganization of actin cytoskeleton at the growing end of the cleavage furrow of Xenopus egg during cytokinesis. J Cell Sci 114, 401–412.
Piekny AJ, Maddox AS (2010). The myriad roles of anillin during cytokinesis. Semin Cell Dev Biol 21, 881–891.
Piekny AJ, Mains PE (2002). Rho-binding kinase (LET-502) and myosin phosphatase (MEL-11) regulate cytokinesis in the early Caenorhabditis elegans embryo. J Cell Sci 115, 2271–2282.
Pollard TD (2010). Mechanics of cytokinesis in eukaryotes. Curr Opin Cell Biol 22, 50–56.
Rappaport R (1996). Cytokinesis in Animal Cells, Cambridge, UK: Cambridge University Press.
Reichl EM, Ren Y, Morphew MK, Delannoy M, Effler JC, Girard KD, Divi S, Iglesias PA, Kuo SC, Robinson DN (2008). Interactions between myosin and actin crosslinkers control cytokinesis contractility dynamics and mechanics. Curr Biol 18, 471–480.
Reinsch S, Karsenti E (1994). Orientation of spindle axis and distribution of plasma membrane proteins during cell division in polarized MDCKII cells. J Cell Biol 126, 1509–1526.
Ren Y, Effler JC, Norstrom M, Luo T, Firtel RA, Iglesias PA, Rock RS, Robinson DN (2009). Mechanosensing through cooperative interactions between myosin II and the actin crosslinker cortexillin I. Curr Biol 19, 1421–1428.
Reymann AC, Martiel JL, Cambier T, Blanchoin L, Boujemaa-Paterski R, Théry M (2010). Nucleation geometry governs ordered actin networks structures. Nat Mater 9, 827–832.
Saarikangas J, Barral Y (2011). The emerging functions of septins in metazoans. EMBO Rep 12, 1118–1126.
Sain A, Inamdar MM, Julicher F (2015). Dynamic force balances and cell shape changes during cytokinesis. Phys Rev Lett 114, 048102.
Schroeder TE (1972). The contractile ring. II. Determining its brief existence, volumetric changes, and vital role in cleaving Arbacia eggs. J Cell Biol 53, 419–434.
Schroeder TE (1973). Actin in dividing cells: contractile ring filaments bind heavy meromyosin. Proc Natl Acad Sci USA 70, 1688–1692.
Sellin ME, Sandblad L, Stenmark S, Gullberg M (2011). Deciphering the rules governing assembly order of mammalian septin complexes. Mol Biol Cell 22, 3152–3164.

Severson AF, Baillie DL, Bowerman B (2002). A Formin Homology protein and a profilin are required for cytokinesis and Arp2/3-independent assembly of cortical microfilaments in C. elegans. Curr Biol 12, 2066–2075.
Shin JH, Mahadevan L, So PT, Matsudaira P (2004). Bending stiffness of a crystalline actin bundle. J Mol Biol 337, 255–261.
Shlomovitz R, Gov NS (2008). Physical model of contractile ring initiation in dividing cells. Biophys J 94, 1155–1168.
Skau CT, Courson DS, Bestul AJ, Winkelman JD, Rock RS, Sirotkin V, Kovar DR (2011). Actin filament bundling by fimbrin is important for endocytosis, cytokinesis, and polarization in fission yeast. J Biol Chem 286, 26964–26977.
Stachowiak MR, Laplante C, Chin HF, Guirao B, Karatekin E, Pollard TD, O'Shaughnessy B (2014). Mechanism of cytokinetic contractile ring constriction in fission yeast. Dev Cell 29, 547–561.
Straight AF, Field CM, Mitchison TJ (2005). Anillin binds nonmuscle myosin II and regulates the contractile ring. Mol Biol Cell 16, 193–201.
Tanaka-Takiguchi Y, Kinoshita M, Takiguchi K (2009). Septin-mediated uniform bracing of phospholipid membranes. Curr Biol 19, 140–145.
Thoresen T, Lenz M, Gardel ML (2011). Reconstitution of contractile actomyosin bundles. Biophys J 100, 2698–2705.
Tse YC, Werner M, Longhini KM, Labbe JC, Goldstein B, Glotzer M (2012). RhoA activation during polarization and cytokinesis of the early Caenorhabditis elegans embryo is differentially dependent on NOP-1 and CYK-4. Mol Biol Cell 23, 4020–4031.
Turlier H, Audoly B, Prost J, Joanny JF (2014). Furrow constriction in animal cell cytokinesis. Biophys J 106, 114–123.
Vale RD, Spudich JA, Griffis ER (2009). Dynamics of myosin, microtubules, and Kinesin-6 at the cortex during cytokinesis in Drosophila S2 cells. J Cell Biol 186, 727–738.
Vavylonis D, Wu JQ, Hao S, O'Shaughnessy B, Pollard TD (2008). Assembly mechanism of the contractile ring for cytokinesis by fission yeast. Science 319, 97–100.
Veigel C, Molloy JE, Schmitz S, Kendrick-Jones J (2003). Load-dependent kinetics of force production by smooth muscle myosin measured with optical tweezers. Nat Cell Biol 5, 980–986.
Verbrugghe KJ, White JG (2004). SPD-1 is required for the formation of the spindle midzone but is not essential for the completion of cytokinesis in C. elegans embryos. Curr Biol 14, 1755–1760.
Vrabioiu AM, Mitchison TJ (2006). Structural insights into yeast septin organization from polarized fluorescence microscopy. Nature 443, 466–469.
Wang Y-l, (2005). The mechanism of cortical ingression during early cytokinesis: thinking beyond the contractile ring hypothesis. Trends Cell Biol 15, 581–588.
Wilson CA, Tsuchida MA, Allen GM, Barnhart EL, Applegate KT, Yam PT, Ji L, Keren K, Danuser G, Theriot JA (2010). Myosin II contributes to cell-scale actin network treadmilling through network disassembly. Nature 465, 373–377.
Wu JQ, Kuhn JR, Kovar DR, Pollard TD (2003). Spatial and temporal pathway for assembly and constriction of the contractile ring in fission yeast cytokinesis. Dev Cell 5, 723–734.
Yang Q, Zhang XF, Pollard TD, Forscher P (2012). Arp2/3 complex-dependent actin networks constrain myosin II function in driving retrograde actin flow. J Cell Biol 197, 939–956.
Yumura S, Ueda M, Sako Y, Kitanishi-Yumura T, Yanagida T (2008). Multiple mechanisms for accumulation of myosin II filaments at the equator during cytokinesis. Traffic 9, 2089–2099.
Zhou M, Wang Y-L (2008). Distinct pathways for the early recruitment of myosin II and actin to the cytokinetic furrow. Mol Biol Cell 19, 318–326.
Zumdieck A, Kruse K, Bringmann H, Hyman AA, Julicher F (2007). Stress generation and filament turnover during actin ring constriction. PLoS One 2, e696.